Journal of Materials Chemistry A

Accepted Manuscript

ROYAL SOCIETY OF CHEMISTRY

www.rsc.org/materialsA

3D hierarchical Co_3O_4@Co_3S_4 nanoarrays as cathode materials for asymmetric pseudocapacitor

Bo Liu,‡[a] Dezhi Kong,‡[a,b] Jun Zhang,[c] Ye Wang,[a] Tupei Chen,[c] Chuanwei Cheng,[b] and Hui Ying Yang[a,*]

[a] Pillar of Engineering Product Development, Singapore University of Technology and Design, 8 Somapah Road, Singapore, 487372

[b] Shanghai Key Laboratory of Special Artificial Microstructure Materials and Technology, School of Physics Science and Engineering, Tongji University, Shanghai 200092, P. R. China

[c] School of Electrical and Electronic Engineering, Nanyang Technological University, Singapore 639798, Singapore

‡ These authors contribute equally to this work.

*Corresponding author. Tel.: +65 6303 6663; Fax: +65 6779 5161. E-mail address: yanghuiying@sutd.edu.sg (H. Y. Yang)

Abstract

Three-dimensional (3D) hierarchical Co_3O_4@Co_3S_4 nanoarrays (NAs) were synthesized *via* a stepwise hydrothermal method involving precipitation and in-situ sulfurization of Co_3O_4 nanoneedle arrays (NNAs). By controlling both anion exchange and ostwald ripening reactions during the sulfurization process, 3D hierarchical Co_3O_4@Co_3S_4 NAs with tailored Co_3S_4 nanostructures have been fabricated as electrode materials for electrochemical capacitor applications. Owing to an interconnected matrix within the 3D architecture, the as-prepared Co_3O_4@Co_3S_4 NAs exhibit excellent electrical conductivity, high specific capacity and high cycling stability. It can deliver a high capacitance of 1284.3 F g^{-1} at 2 mV s^{-1} and maintained a capacitance retention of 93.1 % after 5000 cycles. Moreover, a flexible solid-state

asymmetric supercapacitor (ASC) composed of Co_3O_4@Co_3S_4 NAs as the positive electrode and activated carbon (AC) as the negative electrode exhibited an energy density of 1.5 m Wh cm^{-3} and a power density of 6.1 W cm^{-3} at a high operating voltage of 1.6 V. Our result not only presents the 3D hierarchical nanostructure of Co_3O_4@Co_3S_4 NAs, but it also demonstrates the potential of electrodes for future generation supercapacitors.

Introduction

The large proliferation of advanced electronic devices, such as curved displays, RFID modules, biosensors etc. has stimulated intense research into reliable and efficient energy storage technologies.[1-7] Among the various energy storage technologies, supercapacitors or otherwise known as electrochemical capacitors (EC) are most promising due to the desirable properties. Indeed, supercapacitors exhibit rapid charge/discharge capability, long cycle stability, high power density, and good safety.[8-11] However, suffering from the low energy density, the further applications of supercapacitors are quite limited. To date, there are two strategies to improve the energy density: 1) substitution of carbonaceous materials with pseudocapacitive transition-metal compounds; 2) rational marriage of active materials through smart design and integration.[12]

Pseudocapacitive transition-metal compounds with excellent electrochemical performance have been investigated, such as, cobalt oxides and/or sulfides. They are emerging as promising candidates to provide both high theoretical capacitance and high chemical activity of the metal ions.[13-16] However, the poor capacity retention of cobalt oxide is considered to be the bottleneck to restrict its application as electrode materials. On the one hand, an effective approach to this problem is embedding cobalt oxide with conductive nanostructured carbons.[17-19] On the other hand, construction of 3D hierarchical cobalt oxides/cobalt sulfides nanocomposites *via* smart integration is another typical approach.[20, 21] Among the various cobalt sulfides, β-$CoS_{1.097}$ nanoparticles, Co_9S_8 nanotubes, hollow CoS nanosheet, and flowerlike CoS present

capacitance values of 386 F g^{-1} (20 A g^{-1}), 245 F g^{-1} (2 A g^{-1}), 338.2 F g^{-1} (32.3 A g^{-1}), 521.5 F g^{-1} (10 A g^{-1}), respectively. [22-25] Furthermore, Das *et al.*[26] reported the cross-linked Co_3S_4 nanosheet on Ni@rGO, which delivered a high specific capacitance of 1112.4 F g^{-1} and an improved rate capability. Zhong *et al.*[27] demonstrated the phase transformation synthesis of Co_3S_4 nanosheet arrays using Co_3O_4 template, which exhibited good rate capability as well as a very high specific capacitance of 1081 F g^{-1} at a current density of 1.61 A g^{-1}. However, due to the volumetric swelling and shrinking arising at the pseudocapacitive reaction, the capacitance retention still need to be improved in order to meet the practical demand. Therefore, an optimized design and integration of Co_3O_4 and Co_3S_4 for the Co_3O_4@Co_3S_4 embodiment is supposed to be an attractive cathode material for real application due to their superior electrochemical properties. Nevertheless, the investigation of the hierarchical hybrid Co_3O_4@Co_3S_4 nanostructure is still in the primary stage.

Herein, we report a facile process to fabricate 3D hierarchical Co_3O_4@Co_3S_4 NAs on Ni foam substrate as positive electrode for the flexible and solid-state ASC for first time, where the mesoporous Co_3O_4 nanoneedles were used as highly capacitive 'core' and Co_3S_4 layer were anchored over the core as conductive 'shell'. The smart design presents several superior properties. Firstly, the Co_3S_4 layer were not only used as capacitive materials to enhance the capacitance, but also served as conductive layer to shorten the charge transfer distance. Secondly, the hierarchical architecture involving Co_3O_4 needles coated with interconnected Co_3S_4 whiskers leads to an improved stable

architecture, especially under alkaline electrolyte. Moreover, the core/shell structure can increase contact in an electrolyte, enable the fast redox reaction, and protect the inner Co_3O_4 core as a result of promoting long cycling stability. By advantages of the synergistic contribution from structure composition, the resulting Co_3O_4@Co_3S_4 electrode exhibits a high capacitance of 1284.3 F g^{-1} at 2 mV s^{-1} with capacitance retention of 93.1 %. Moreover, a solid asymmetric supercapacitor composed of Co_3O_4@Co_3S_4//AC exhibits excellent electrochemical performance with energy and power density of 1.5 m Wh cm^{-3} at 6.1 W cm^{-3}, which maintains the capacity even after 6000 cycles with excellent capacity retention of 90.2 %.

Experimental Section

Synthesis of Co_3O_4 NNAs.

Co_3O_4 nanoneedle arrays were prepared using a simple one-step hydrothermal process. In a typical procedure, 0.58 g of cobalt nitrate hexahydrate ($Co(NO)_3 \cdot 6H_2O$), 0.6 g ammonium fluoride (NH_4F) and 1.2 g urea were dissolved in 80 ml deionized (DI) water. After stirring for 30 min, the solution was then transferred into a 100 ml Teflon-lined autoclave. A piece of Ni foam (3×7 cm^2) was first treated with 3 M HCl solution for 30 min to remove the oxides, and then washed thoroughly with DI water and absolute ethanol to remove the impurities from its surface. The Ni foam was quickly dried and weighed before immersing into the reaction solution, and then it was sealed and maintained at 130 ℃ for 9 h followed by cooling down to room temperature naturally. The resulting pink Co-based carbonate hydroxide on Ni foam was collected and vigorously washed with DI water and absolute ethanol to remove ion and possible remnants. Then the product was dried in air at 60 ℃ for 6 h and annealed at 400 ℃ for 4 h with a ramping rate of 5 ℃/min to completely transform pink Co-based carbonate hydroxide into black Co_3O_4 NNAs.

Synthesis of Co_3O_4@Co_3S_4 NAs.

The Co_3O_4@Co_3S_4 NAs were synthesized *via* a simple hydrothermal process with different duration. In detail, 0.46 g $Na_2S \cdot 2H_2O$, 80 ml DI water and the as-prepared Co_3O_4 NNAs on Ni foam were placed into a 100 ml Teflon-lined autoclave. The temperature was maintained at 90 ℃ for 12 h, 24 h, and 36 h, and then cooled down to room temperature naturally. Next, the as-prepared samples were collected, dried

and annealed in argon atmosphere before testing. The chemical reaction equation for Co_3S_4 can be listed as bellow:

$$Co_3O_4 + 8H_2O + 4S^{2-} \leftrightarrow Co_3S_4 + 4H_2O + 8OH^- \quad (1)$$

Characterization

The morphology and size of the samples was investigated using a scanning electron microscopy (SEM, JSM-7600F, JEOL Inc., Japan). Meanwhile, the chemical composition was performed on the same SEM equipped with an energy-dispersive X-ray (EDX) spectroscopy (Oxford INCA EDS). The morphology and structure of the samples were characterized by a transmission electron microscopy (TEM, JEM-2010, JEOL Inc., Japan). The powder was ultrasonicated from the Ni foam for X-ray diffraction (XRD) characterization on Bruker, D8 Advance-Eco diffractometer with Cu-Kα radiation (λ≈1.54178 Å). Raman spectra of Co_3O_4@Co_3S_4 NAs were detected *via* a confocal Raman system with the 532 nm laser excitation source (WITec Instruments Corp, Germany). The chemical valence states of Co_3O_4@Co_3S_4 NAs were investigated with X-ray photoelectron spectroscopy (XPS, PHI Quantera II, Physical Electronics, Adivision of ULCAV-PHI). The content of Co_3S_4 in the nanocomposites was measured by thermogravimetric analysis (TGA, Shimadzu, DTG-60) under air flow with a heating rate of 10 ℃ min^{-1} from room temperature to 950 ℃. The specific surface area of Co_3O_4 NNAs and Co_3O_4@Co_3S_4 NAs was carried out by N_2 physisorption at 77 K using the Brunauer–Emmett–Teller (BET, TriStar II 3020, Micromeritics) method.

Electrochemical measurements

The electrochemical testing was carried out by an electrochemical workstation (VMP3, Bio-Logic, France) in a 3.0 M aqueous KOH electrolyte by a typical three-electrode configuration. The Co_3O_4 NNAs and Co_3O_4@Co_3S_4 NAs were used as the working electrodes, platinum foil as the counter electrode, and saturated calomel electrode (SCE) as the reference electrode. The as-synthesized Co_3O_4 NNAs (~ 1.95 mg cm^{-2}) and Co_3O_4@Co_3S_4 NAs (~ 2.28 mg cm^{-2}) on Ni foam were directly used as electrode without adding of binder. Cyclic voltammetry (CV) was performed between -0.2 - 0.6 V at 2, 5, 10, 20, 30, 50 mV s^{-1} together with galvanostatic charging/discharging tested between -0.1 - 0.4 V at 2, 4, 10, 20 A g^{-1}, respectively. Moreover, electrochemical impedance spectroscopy (EIS) testing was conducted with frequencies ranging from 0.01 to 10000 Hz. The working electrodes immersed in the electrolyte was 1 cm^2 in nominal area. Correspondingly, the specific capacitance were calculated with:

$$C_s = \frac{\int_{-V}^{V} i \times dV}{2 \times v \times \Delta V \times m} \quad (2)$$

where C_s is the specific capacitance, $\int_{-V}^{V} i \times dV$ is the integrated area of CV curve, v is the scan rate, ΔV is the potential range in CV figure, and m is the loading mass of active materials on Ni foam.

The flexible ASC was fabricated using Co_3O_4@Co_3S_4 as positive electrode, AC as negative electrode, and the PVA-KOH as solid-state electrolyte. The AC electrodes were fabricated *via* mixing AC, carbon black, and PVDF with a mass ratio of 8:1:1, and pasting the slurry onto Ni foam (3×7 cm^2). The semi-finished AC electrodes were subsequently dried in vacuum over at 80 ℃ for 6 h. Then the PVA-KOH electrolyte

was prepared *via* dissolving 6 g PVA, 3 g KOH in 70 ml DI water under 100 ℃. The PVA-KOH solution were directly coated onto the electrodes uniformly and waited for naturally drying. After the two electrodes were assembled, the PVA-KOH functioned as electrolyte and separator due to the all-solid-state characteristic. CV and galvanostatic charging/discharging were performed both between 0 and 1.6 V at different scan rates and current densities, respectively.

Results and discussion

The typical synthesis approach of 3D Co_3O_4@Co_3S_4 NAs involves hydrothermal precipitation, annealing, and second hydrothermal sulfurization process, as schematically shown in **Fig. 1a.** Initially, the magenta Co-based carbonate hydroxides were synthesized on Ni foam *via* precipitation reaction of the three kinds of soluble salts ($Co(NO_3)_2{\cdot}6H_2O$, NH_4F and Urea). Afterwards, Co_3O_4 NNAs were generated directly on the Ni foam substrate *via* a simple annealing process. Consequently, the as-obtained Co_3O_4 NNAs were treated with the sulfurization process and thus the hierarchical 3D Co_3O_4@Co_3S_4 NAs were prepared. The optical images of different reaction stages are as shown in **Fig. S1**, showing the Ni foam after the acid treatment (a), Co-based carbonate hydroxide (b), Co_3O_4 NNAs (c), and Co_3O_4@Co_3S_4 NAs (d), respectively. The SEM images of Co_3O_4 NNAs and Co_3O_4@Co_3S_4 NAs present the specific structure after different process. Of note, **Fig. 1b** shows that the 1D Co_3O_4 needles were grown with various angles, clustering on Ni foam evenly (as shown in the inset), which indicates that the structure was maintained during the annealing process. Moreover, **Fig. 1c** and its inset shows the Co_3O_4 needles were coated by one layer of Co_3S_4 uniformly, exhibiting a rougher morphology when compared to the Co_3O_4 NNAs. Furthermore, the energy dispersive X-ray (EDX) spectroscopy and elemental mapping were performed to determine the constituent distribution of Co_3O_4 and Co_3S_4, which is as shown in **Fig. S2.** Noting that, the micrometer-sized Co_3O_4 clusters assembled together with homogeneous distribution of Co and S elements on the surface.

The comparative study on the morphologic and structural properties of the Co_3O_4 NNAs and Co_3O_4@Co_3S_4 NAs samples was carried out using SEM and TEM technologies. From **Fig. 2a**, Co_3O_4 NNAs is composed of 1D needles with an uneven surface texture, clearly exhibiting porous and grainy characteristics. In contrast, from **Fig. 2b**, the Co_3S_4 whiskers with high density grew uniformly on the needles, forming a puffing shell structure. As expected, TEM characterization shows the 1D porous texture of Co_3O_4 NNAs and 3D hierarchical nanostructure of Co_3O_4@Co_3S_4 NAs in detail. **Fig. 2c** shows each needle is consisted of Co_3O_4 particles, which resulted from the release of H_2O and CO_2 gas during pyrolysis. Moreover, the insets of **Fig. 2c** demonstrate a lattice spacing of *ca.* 0.47 nm which is corresponding to (111) plane of Co_3O_4.[28] Meanwhile, Fast Fourier Transform (FFT) pattern confirms these Co_3O_4 needles are single-crystalline. Noting that, the porous and crystalline needles show a specific structure that could be used as template for nucleation and rapid growth of Co_3S_4, which is also favorable for electrochemical energy storage. Comparatively, **Fig. 2d** shows Co_3O_4@Co_3S_4 NAs had a peculiar core/shell structure with quasi-transparent Co_3S_4 'shell' formed on Co_3O_4 'core'. Noted from the insets of this figure, it is seen that the Co_3O_4@Co_3S_4 NAs are single-crystalline with the lattice spacing of 0.19 nm which is indexed to the (422) interplanar distance of Co_3S_4.[29]

The chemical composition and crystal structures of the as-prepared Co_3O_4 NNAs and Co_3O_4@Co_3S_4 NAs were verified by XRD and Raman spectroscopy. **Fig. 3a** shows the XRD peaks of Co_3O_4 NNAs were well indexed to the standard XRD pattern of spinel Co_3O_4 (JCPDS card no. 42-1467).[30] In contrast, **Fig. 3b** shows the XRD peaks

of Co_3O_4@Co_3S_4 NAs can be assigned to the standard XRD pattern of spinel Co_3S_4 (JCPDS card no. 19-0367).[31] Of note, the pronounced peaks at 32.1 degree are attributed to the superposition of Co_3O_4 and Co_3S_4 diffraction peaks [32, 33]. No extra peaks were detected, indicating the high purity of the sample. Besides, **Fig. 3c** shows the Raman peaks at 196, 483, 523, 621, and 691 cm^{-1} are well indexed to the characteristic vibration modes of Co_3O_4, corresponding to the F_{2g}, E_g, F_{2g}, F_{2g}, and A_{1g} in Raman spectrum, respectively.[34] In addition, **Fig. 3d** demonstrates the specific peaks of Co_3O_4 (marked as "#") and Co_3S_4 (marked as "*") in Co_3O_4@Co_3S_4 composites, which can be well attributed to vibration modes of each composition.

The chemical oxidation states of the samples have been investigated using XPS system, and the results are as shown in **Fig. 4. Fig. 4a** demonstrates that the four elements (Co, O, S, and C) were characterized in the XPS full spectrum of Co_3O_4@Co_3S_4 NAs. In the XPS elemental spectrum of Co_3O_4@Co_3S_4 NAs, **Fig. 4b** shows that the two distinct peaks at binding energy of 780.8 and 796.2 eV with spin-orbital splitting of 15.2 eV were observed in the Co 2p core level spectrum, which is in accordance with the Co $2p_{3/2}$ and Co $2p_{1/2}$ in Co_3O_4 and Co_3S_4, respectively.[35] Further deconvolution demonstrates the presence of two chemical distinct species: Co^{3+} and Co^{2+}.[36] Moreover, the O 1s core level spectrum (**Fig. 4c**) shows three components, corresponding to oxygen atoms in the hydroxyl group (530.7eV), absorbed water (532.7eV), as well as the one in the Co_3O_4 (529.8eV), respectively.[37] Besides, the S can be further identified by the two distinct 2p peaks at 162.0 eV and 163.1 eV, as shown in **Fig. 4d**.[38] Additionally, the mass content of Co_3S_4

in the Co_3O_4@Co_3S_4 examined by thermogravimetric analysis (TGA, **Fig. S3a**) is about 80%. Meanwhile, the specific surface area of Co_3O_4 NNAs and Co_3O_4@Co_3S_4 NAs are calculated to be 43.8 m^2 g^{-1} and 60.2 m^2 g^{-1} from the BET analysis, respectively, as indicated in **Fig. S3b**.

In order to unveil the effect of sulfurization time, a series of control experiments based on various sulfurization time were carried out. With the less hydrothermal time (*ca.* 12 h), it can be seen that only a trace of Co_3S_4 flakes formed at the tip (**Fig. 5a and 5b**), which could be the result of low nucleation energy in the initial stage.[39] With the hydrothermal reaction time was increased to 24 h, the morphology got rougher with more Co_3S_4 nanowhiskers formed on the Co_3O_4 needles surface as shown in **Fig. 5c**. As the vertical and planar distribution of these whiskers, the **Fig. 5d** shows the pristine Co_3O_4 needles are interconnected densely. With the reaction time increased to 36 h, Co_3S_4 flakes with high density were obtained and occupied the primary surface area of Co_3O_4 needles (**Fig. 5e**). The Co_3O_4 nanowires are overwrapped by the Co_3S_4 flakes as indicated from **Fig. 5f**. Consequently, Co_3S_4 content gradually increased with the extension of sulfurization time, corresponding to the XRD and Raman plots (**Fig. S4**).

According to the results above, a possible mechanism for the growth of Co_3S_4 is summarized as bellow. When Co_3O_4 needles were grown on Ni foam, S^{2-} in Na_2S solution react with Co_3O_4 *via* infiltrating into the needle through mesopores, and the massive growth of Co_3S_4 whiskers over Co_3O_4 surface is a result of outward diffusion of Co^{2+} ions to be faster than the inward diffusion of S^{2-} ions.[40] Therefore, once the

nucleation center was generated, it triggered the growth of Co_3S_4 nanoparticles at the vertical and planar direction. Meanwhile, if hydrothermal reaction is kept for a longer time, the reorganization of Co_3S_4 nanoparticles occurs followed by the orientation growth of Co_3S_4 flakes with high density. Therefore, the growth mechanism of Co_3S_4 whiskers could be attributed to the anion exchange reaction (AER) at the first stage and Ostwald ripening mechanism at the second stage.[26]

Electrochemical charge storage performance of the as-synthesized specimens were first investigated by taking them as working electrodes for pseudocapacitors with a typical three-electrode configuration in 3 M KOH alkaline aqueous electrolyte, with Pt foil and saturated calomel electrode (SCE) as counter electrode and reference electrode, respectively. When tested at a scan rate of 30 $mV \cdot s^{-1}$ in the potential range of -0.2 to 0.6 V (vs. SCE), all samples (Co_3O_4@Co_3S_4 12 h, Co_3O_4@Co_3S_4 24 h, Co_3O_4@Co_3S_4 36 h and pristine Co_3O_4) presented a categories of pseudocapacitive CV curves (as shown in **Fig. 6a**). Of note, the contribution from Ni foam can be negligible due to the small integrated area. Meanwhile, the CV curves of the Co_3O_4@Co_3S_4 electrodes exhibit much higher current densities than those of pristine Co_3O_4 electrodes, which shows a significant improvement of capacitance after sulfurization. The improved capacitance resulted from the increased reactive sites due to plenty of ultrathin Co_3S_4 whiskers wrapped over the Co_3O_4 building-block effectively. Such integration not only ensured the utility of superior properties of each composition, but it also enhanced the 3D hierarchical structure which in turn improved the electrochemical performance. As shown in **Fig. 6b**, the galvanostatic

charging/discharging measurements of samples were further conducted at current density of 4 $A \cdot g^{-1}$. As expected, the sulfurized electrodes exhibited much longer discharging time than raw Co_3O_4 electrode, indicating the ultrathin (quasi-transparence), large-size (hundreds of nanometers), and stable (ultrasonic tolerance at TEM sample preparation) characteristics of Co_3S_4 is favorable for electrochemical storage. Furthermore, Co_3O_4@Co_3S_4 24 h shows the highest specific capacitance of 1284.3 F g^{-1} at scan rates of 2 mV s^{-1}.

In order to study the influence of the scan rates on the electrochemical performance of Co_3O_4@Co_3S_4 24 h, the CV performance of samples were performed at various scan rates ranging from 2 to 50 mV s^{-1}. A pair of redox peaks are clearly observed in **Fig. 6c**, which is mainly attributed to the pseudocapacitive mechanism, such as Co^{2+}/Co^{3+} redox couple. In case of Co_3O_4, the electrochemical reactions are shown below: [41, 42]

$$Co_3O_4 + OH^- + H_2O \leftrightarrow 3CoOOH + e^- \quad (3)$$

$$CoOOH + OH^- \leftrightarrow CoO_2 + H_2O + e^- \quad (4)$$

In addition, the positions of cathodic and anodic peaks shifted towards more anodic and cathodic directions at the higher scan rates, and the current density of the curves get increased, indicating the fast ionic and electronic transfer speed over the electrodes surface at high scan rates. In order to get more information about the performance of the Co_3O_4@Co_3S_4 24 h electrodes, the galvanostatic charging/discharging measurements were further carried out at various current densities in the voltage range of -0.1-0.4 V (vs. SCE). As shown in **Fig. 6d**, all the galvanostatic charging/discharging plots show a typical nonlinear behavior at different

current densities ranging from 1 to 20 A g^{-1}, exhibiting pseudocapacitive nature of the samples. In contrast, the CV (2 to 50 mV s^{-1}) and charging/discharging (1 to 20 A g^{-1}) curves of Co_3O_4, Co_3O_4@Co_3S_4 12 h, and Co_3O_4@Co_3S_4 36 h were presented in **Fig. S5**. These results reveal that the 3D hierarchical Co_3O_4@Co_3S_4 NAs exhibited enhanced electrochemical performance compared to pristine Co_3O_4 NNAs, indicating that the Co_3S_4 NAs does not only act as a pseudocapacitive shell for improving capacitance, but rather some sort of interaction role of Co_3S_4 is there between Co_3O_4, Co_3S_4, and electrolyte, resulting in the improved electrochemical activity. In this design, the Co_3S_4 layer plays a dual role: on one hand, it increases the reaction sites and boost the more ions and electrons transfer in electrolyte/electrode materials region; on the other hand, it enhanced the Co_3O_4 NNAs structure by coating a layer of Co_3S_4, which protected the morphology of Co_3O_4 nanowires from damaging in applications.

The electrochemical impedance spectroscopy (EIS) measurements on the Co_3O_4, Co_3O_4@Co_3S_4 12 h, Co_3O_4@Co_3S_4 24 h, and Co_3O_4@Co_3S_4 36 h electrodes were performed to understand the electrochemical reaction kinetics. Noted from the **Fig. 6e**, it is demonstrated that the Nyquist plots of the EIS spectra show a similar semicircle at high frequency range and a spike at low frequency range. Especially, in a high frequency area, the intercept to the x axis represents the bulk resistance (R_e), while the semicircle corresponds to the double-layer capacitance and charge-transfer resistance (R_{ct}). The R_e resistance (0.59 Ω) of Co_3O_4@Co_3S_4 24 h electrodes is smaller than that of pristine Co_3O_4 electrodes (0.79 Ω), which is attributed to the decoration of Co_3S_4 nanowhiskers facilitating the infiltration of OH^- to the Co_3O_4

'core'.[43] The R_{ct} of the hybrid Co_3O_4@Co_3S_4 24 h electrodes (0.97 Ω) is lower than Co_3O_4@Co_3S_4 36 h (1.44 Ω), indicating the excessive coating Co_3O_4 with Co_3S_4 impede the ionic transfer. In this regard, the pores or voids inside the arrays are beneficial for the electrolyte infiltration in the core/shell structure. Meanwhile the interconnected nature of Co_3O_4 enables effective ion and electron transportation, indicating the enhancement of the overall electrochemical properties. Likewise, compared with the Co_3O_4@Co_3S_4 12 h and Co_3O_4@Co_3S_4 24 h, further increase the sulfurization time to 36 h result in capacitance degradation, exhibiting deteriorated access of electrolyte diffusion to the inner core of Co_3O_4. In other words, the increased resistance originated from the deteriorated morphology of Co_3S_4 layer, which made the electrochemical performance of hybrid structure to decrease rather than improve. The calculated specific capacitance based on the CV curves are presented in **Fig. 6f**. The Co_3O_4@Co_3S_4 24 h electrode can deliver specific capacitances of 1284.3, 631.9, 425.1, 311.1, 283.7, and 206.7 F g^{-1} at scan rates of 2, 5, 10, 20, 30, 50 mV s^{-1}, respectively, which is much higher than the other Co_3O_4@Co_3S_4 electrodes and the pristine Co_3O_4 electrodes at the same scan rates, as indicated in **Table 1**. Furthermore, Co_3O_4@Co_3S_4 24 h electrodes still can keep the capacitance retention of 93.1 % after 5000 cycles at current density of 4 A g^{-1} demonstrating the excellent cycling stability, as shown in **Fig. S6a**. Moreover, the galvostatic charging/discharging curves in **Fig. S6b** further confirmed little performance degradation of Co_3O_4@Co_3S_4 24 h electrodes.

To further investigate the practical application of this design, a full-cell of 1.5×6 cm^2

asymmetric supercapacitor was prepared using AC as negative electrode and Co_3O_4@Co_3S_4 24 h as positive electrode, and the typical PVA/KOH as gel-like electrolyte (denoted as Co_3O_4@Co_3S_4//AC ASC). Before assembling, the CV comparison of both AC electrodes and Co_3O_4@Co_3S_4 electrodes were tested at the scan rate of 30 mV s^{-1} in a three-electrode system, as shown in **Fig. S7a**. According to the charge balance $q^+ = q^-$, the mass balance between the positive and negative electrode can be obtained *via* $m^-/m^+ = (C^+ \times \Delta V^+)/(C^- \times \Delta V^-)$, where the C^+ and C^- is the capacitance of respective electrode, ΔV^+ and ΔV^- is the corresponding voltage range for charging-discharging process, hence the loading mass of AC electrode is ~3.5 mg/cm^2 after balance. From **Fig. S7b**, the as-prepared asymmetric supercapacitor was tested at various scan rates ranging from 2 to 20 mV s^{-1} in the potential window of 0 to 1.6 V. The quasi-rectangular CV geometry indicated the obvious redox characteristic, which is quite consistent with the three electrode testing results. With the higher scan rate (10 mV s^{-1}), the curve differed slightly from the previous results but remained quasi-rectangular shape, showing the capability for high power delivery. In addition, it is seen from **Fig. S8a and b** that both the CV and charging/discharging curves at different potential windows were collected. Significantly, the calculated volumetric capacitance (based on the volume of the entire device) increases from 0.71 to 1.28 F cm^{-3} when operation voltage increases from 0.8 to 1.6 V (**Fig. S8c**). Therefore, according to formula (7), the energy density of the ASC was improved by 750 %.[44] Galvanostatic charging/discharging testing of Co_3O_4⊙Co_3S_4//AC ASCs under various current densities are shown in **Fig. 7a**, where

the charging-discharging curves are almost symmetric to each other, exhibiting good capacitive characteristic. Furthermore, the cycling performance of Co_3O_4⊙Co_3S_4//AC ASCs is also a key factor to evaluate the supercapacitor performance, and thus the ASC device was cycled between 0 - 1.6 V at a current density of 20 mA cm^{-2} for 6000 cycles. As can be seen in **Fig. 7b**, the result shows a very small capacity decay after 6000 cycles, which is mainly due to the deterioration of gel-like electrolyte during the cycling process.[45] Besides, the inset shows the first and last 6 charging-discharging cycles, where the slight deformation indicates the good capacitive characteristic. Noted from the figure, the capacity retention of 90.2 % after 6000 cycles indicated the excellent capacity retention of the sample. The energy density and power density are two key parameters for evaluating practical performance of the supercapacitor, which can be achieved from the following equations:[40]

$$\mathrm{E} = \frac{1}{2} \times C \times V^2 \quad (7)$$

$$\mathrm{P} = E/t \quad (8)$$

Where C is the capacitance of ASCs, V is the operation voltage window in volts, and t is the time. Meanwhile, the Ragone plot descripting the relation between energy and power density of the Co_3O_4⊙Co_3S_4//AC ASCs was shown in **Fig. 7c**. Impressively, the ASCs can achieve a maximum energy density of 1.5 mW h cm^{-3} at 6.1 W cm^{-3} and 0.8 mW h cm^{-3} at 64.1 W cm^{-3}, which is much higher than the previous results of asymmetric supercapacitors.[46-49] In order to evaluate the potential of Co_3O_4⊙Co_3S_4//AC ASCs for flexible energy storage under real condition, the CV curves of the device at 20 mV s^{-1} were collected under bending, normal, and twist

condition in **Fig. S8d**, revealing its excellent mechanical stability. To further confirm the Co_3O_4⊙Co_3S_4//AC ASCs for real application, the devices were used to drive a DC motor and several 5 mm diameter LEDs, as shown in **Fig. 7 d1, d2**. The ASCs could successfully drive the motor (3.7 V, 0.45 W) for 5 min or power five LEDs (0.8 V, 10 mA) for 10 min after full charging.

Conclusion

In summary, we have demonstrated a 3D hierarchical Co_3O_4@Co_3S_4 NAs on Ni foam as positive electrode for a flexible solid-state ASCs application. Owing to integration of Co_3S_4 nanowhiskers over the Co_3O_4 surface, the electrochemical performance of metal oxides after sulfurization gets enhanced with high specific capacitance superior rate capability and excellent cycling stability. The 3D architecture consisting of Co_3S_4 as interconnected layer not only improves the chemical composition, but tunes the morphology with smart distribution of active materials, indicating convenience of in-situ sulfurization for fabricating the positive materials for supercapacitor application. Noteworthy, the capacity retention after 6000 cycles turns out to be as high as 90.2 %, which highly competitive for daily life application. The as-prepared asymmetric two-electrode pseudocapacitor was further evaluated as power source to drive LEDs and a DC motor for a long time after full charging, indicating the Co_3O_4@Co_3S_4 NAs are a type of promising candidate for next generation high-performance flexible and lightweight supercapacitors. This facile electrode preparing process may also open up a new opportunity for fabricating other metal oxide/sulfide electrodes.

Acknowledgements

This work is supported by SUTD Digital Manufacturing and Design (DManD) center and SUTD-MIT international design center.

References

1. J. Bae, M. K. Song, Y. J. Park, J. M. Kim, M. Liu and Z. L. Wang, *Angew. Chem. Int. Ed. Engl.*, 2011, **50**, 1683-1687.
2. F. Meng and Y. Ding, *Adv. Mater.*, 2011, **23**, 4098-4102.
3. G. P. Xiong, C. Z. Meng, R. G. Reifenberger, P. P. Irazoqui and T. S. Fisher, *Adv. Energy Mater.*, 2014, **4**, 1300515
4. C. Meng, C. Liu, L. Chen, C. Hu and S. Fan, *Nano Lett.*, 2010, **10**, 4025-4031.
5. Y. G. Zhu, Y. Wang, Y. Shi, J. I. Wong and H. Y. Yang, *Nano Energy*, 2014, **3**, 46-54.
6. Z. Zhang, F. Xiao, L. Qian, J. Xiao, S. Wang and Y. Liu, *Adv. Energy Mater.*, 2014, **4**, 1400064.
7. V. L. Pushparaj, M. M. Shaijumon, A. Kumar, S. Murugesan, L. Ci, R. Vajtai, R. J. Linhardt, O. Nalamasu and P. M. Ajayan, *Proc. Natl. Acad. Sci. USA*, 2007, **104**, 13574-13577.
8. Z. S. Wu, G. M. Zhou, L. C. Yin, W. Ren, F. Li and H. M. Cheng, *Nano Energy*, 2012, **1**, 107-131.
9. C. Long, T. Wei, J. Yan, L. Jiang and Z. Fan, *ACS Nano*, 2013, **7**, 11325-11332.
10. Y. Zhang, W. Sun, X. Rui, B. Li, H. T. Tan, G. Guo, S. Madhavi, Y. Zong and Q. Yan, *Small*, 2015, **11**, 3694-3702.
11. Q. Wang, L. Jiao, H. Du, Y. Si, Y. Wang and H. Yuan, *J. Mater. Chem. A.*, 2012, **22**, 21387.
12. D. Z. Kong, J. S. Luo, Y. L. Wang, W. N. Ren, T. Yu, Y. S. Luo, Y. P. Yang and C. W. Cheng, *Adv. Funct. Mater.*, 2014, **24**, 3815-3826.
13. D. Lan, Y. Chen, P. Chen, X. Chen, X. Wu, X. Pu, Y. Zeng and Z. Zhu, *ACS Appl Mater Interfaces*, 2014, **6**, 11839-11845.
14. Q. Guan, J. Cheng, B. Wang, W. Ni, G. Gu, X. Li, L. Huang, G. Yang and F. Nie, *ACS Appl Mater Interfaces*, 2014, **6**, 7626-7632.
15. M. Qorbani, N. Naseri and A. Z. Moshfegh, *ACS Appl Mater Interfaces*, 2015, **7**, 11172-11179.
16. S. J. Bao, C. M. Li, C. X. Guo and Y. Qiao, *J. Power Sources*, 2008, **180**, 676-681.
17. Y. G. Zhu, Y. Wang, Y. M. Shi, Z. X. Huang, L. Fu and H. Y. Yang, *Adv. Energy Mater.*, 2014, **4**, 1301788.
18. Y. Liang, M. G. Schwab, L. Zhi, E. Mugnaioli, U. Kolb, X. Feng and K. Mullen, *J. Am. Chem. Soc.*, 2010, **132**, 15030-15037.
19. J.-Y. Lin, S.-Y. Tai and S.-W. Chou, *J. Phys. Chem. C.*, 2013, **118**, 823-830.
20. D. Kong, C. Cheng, Y. Wang, J. I. Wong, Y. Yang and H. Y. Yang, *J. Mater. Chem. A.*, 2015, **3**, 16150-16161.
21. S. Lichusina, A. Chodosovskaja, K. Leinartas, A. Selskis and E. Juzeliunas, *J. Solid State Electrochem.*, 2010, **14**, 1577-1584.
22. B. Qu, Y. Chen, M. Zhang, L. Hu, D. Lei, B. Lu, Q. Li, Y. Wang, L. Chen and T. Wang, *Nanoscale*, 2012, **4**, 7810-7816.
23. H. Z. Wan, X. Ji, J. J. Jiang, J. W. Yu, L. Miao, L. Zhang, S. W. Bie, H. C. Chen and Y. J. Ruan, *J. Power Sources*, 2013, **243**, 396-402.
24. Z. S. Yang, C. Y. Chen and H. T. Chang, *J. Power Sources*, 2011, **196**, 7874-7877.
25. F. L. Luo, J. Li, H. Y. Yuan and D. Xiao, *Electrochim. Acta*, 2014, **123**, 183-189.
26. D. Ghosh and C. K. Das, *ACS Appl Mater Interfaces*, 2015, **7**, 1122-1131.
27. Q. Chen, H. Li, C. Cai, S. Yang, K. Huang, X. Wei and J. Zhong, *RSC Advances*, 2013, **3**, 22922.
28. C. H. Kuo, W. Li, W. Song, Z. Luo, A. S. Poyraz, Y. Guo, A. W. Ma, S. L. Suib and J. He, *ACS Appl Mater Interfaces*, 2014, **6**, 11311-11317.

29. J. H. Zhong, A. L. Wang, G. R. Li, J. W. Wang, Y. N. Ou and Y. X. Tong, *J. Mater. Chem. A.*, 2012, **22**, 5656-5665.
30. O. Knop, K. Reid, Sutarno and Y. Nakagawa, *Can. J. Chem.*, 1968, **46**, 3463-3476.
31. S. Xiong, C. Yuan, X. Zhang, B. Xi and Y. Qian, *Chem. Eur. J.*, 2009, **15**, 5320-5326.
32. M. Paterson, *J. Appl. Phys.*, 1952, **23**, 805-811.
33. W. Huang, H. Zhang, Y. Huang, W. Wang and S. Wei, *Carbon*, 2011, **49**, 838-843.
34. Y. Liu, C. Xiao, M. Lyu, Y. Lin, W. Cai, P. Huang, W. Tong, Y. Zou and Y. Xie, *Angew. Chem. Int. Ed. Engl.*, 2015, **54**, 11231-11235.
35. J. Cui, X. Zhang, L. Tong, J. Luo, Y. Wang, Y. Zhang, K. Xie and Y. Wu, *J. Mater. Chem. A.*, 2015, **3**, 10425-10431.
36. H. Xia, D. Zhu, Z. Luo, Y. Yu, X. Shi, G. Yuan and J. Xie, *Scientific reports*, 2013, **3**.
37. Y. Chu, J. Feng, Y. Qian and S. Xiong, *RSC Advances*, 2015, **5**, 40899-40906.
38. Q. Wang, L. Jiao, H. Du, Y. Si, Y. Wang and H. Yuan, *J. Mater. Chem. A.*, 2012, **22**, 21387-21391.
39. J. Liu, J. Jiang, C. Cheng, H. Li, J. Zhang, H. Gong and H. Fan, *Adv. Mater.*, 2011, **23**, 2076-2081.
40. X. Xia, C. Zhu, J. Luo, Z. Zeng, C. Guan, C. F. Ng, H. Zhang and H. J. Fan, *Small*, 2014, **10**, 766-773.
41. C. Zhou, Y. Zhang, Y. Li and J. Liu, *Nano Lett.*, 2013, **13**, 2078-2085.
42. X. W. Lou, D. Deng, J. Y. Lee and J. Feng, *Adv. Mater.*, 2008, **20**, 258.
43. J. Liu, C. Cheng, W. Zhou, H. Li and H. J. Fan, *Chem Commun (Camb)*, 2011, **47**, 3436-3438.
44. Z. J. Fan, J. Yan, T. Wei, L. J. Zhi, G. Q. Ning, T. Y. Li and F. Wei, *Adv. Funct. Mater.*, 2011, **21**, 2366-2375.
45. D. Kong, C. Cheng, Y. Wang, J. I. Wong and Y. Yang, *J. Mater. Chem. A.*, 2015, **3**, 16150-16161.
46. J. Xu, Q. Wang, X. Wang, Q. Xiang, B. Liang, D. Chen and G. Shen, *ACS Nano*, 2013, **7**, 5453-5462.
47. M. F. El-Kady, V. Strong, S. Dubin and R. B. Kaner, *Science*, 2012, **335**, 1326-1330.
48. X. Lu, M. Yu, G. Wang, T. Zhai, S. Xie, Y. Ling, Y. Tong and Y. Li, *Adv. Mater.*, 2013, **25**, 267-272.
49. P. Yang, X. Xiao, Y. Li, Y. Ding, P. Qiang, X. Tan, W. Mai, Z. Lin, W. Wu and T. Li, *ACS nano*, 2013, **7**, 2617-2626.

Figures

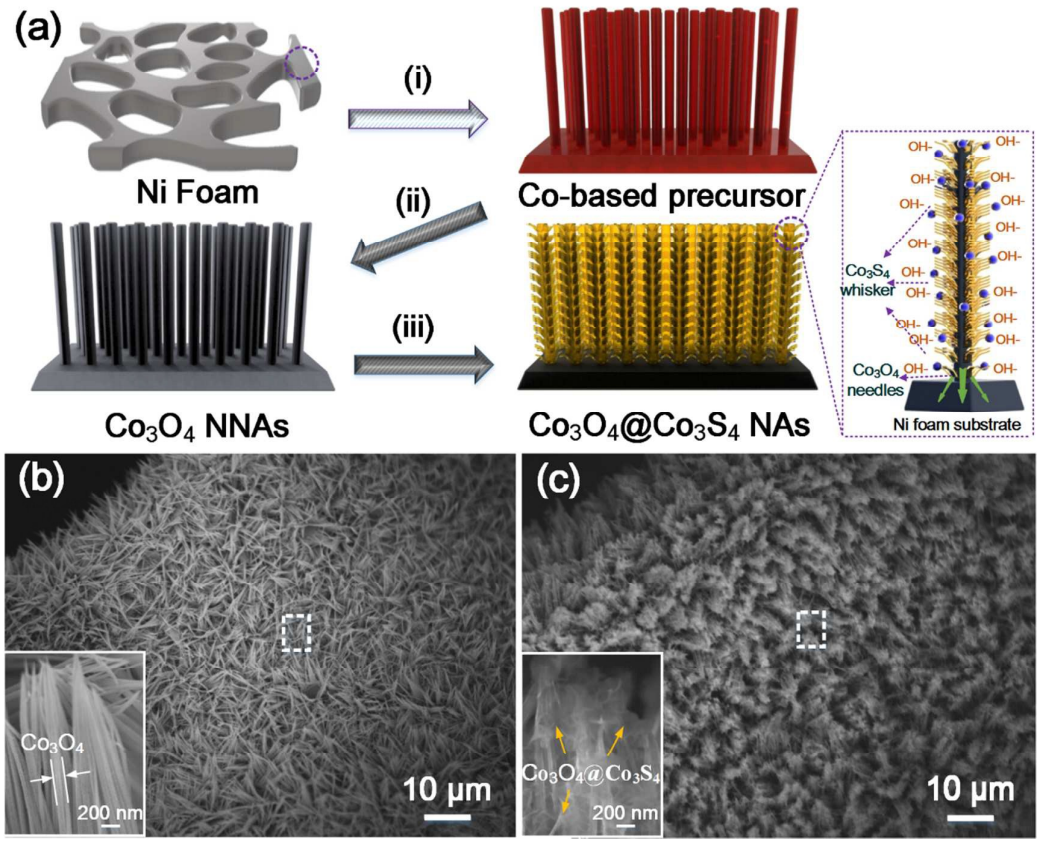

Fig. 1 (a) Schematic illustration of the synthesis process for Co_3O_4@Co_3S_4 NAs on Ni foam: (i) hydrothermal precipitation process; (ii) annealing process; (iii) hydrothermal sulfurization process; SEM images of (b) Co_3O_4 NNAs and (c) Co_3O_4@Co_3S_4 NAs. Insert in (b) is Co_3O_4 needles with an average diameter of 80 nm; moreover, the hybrid hierarchical nanostructure obtained after 24 h in insert (c) is web-like network.

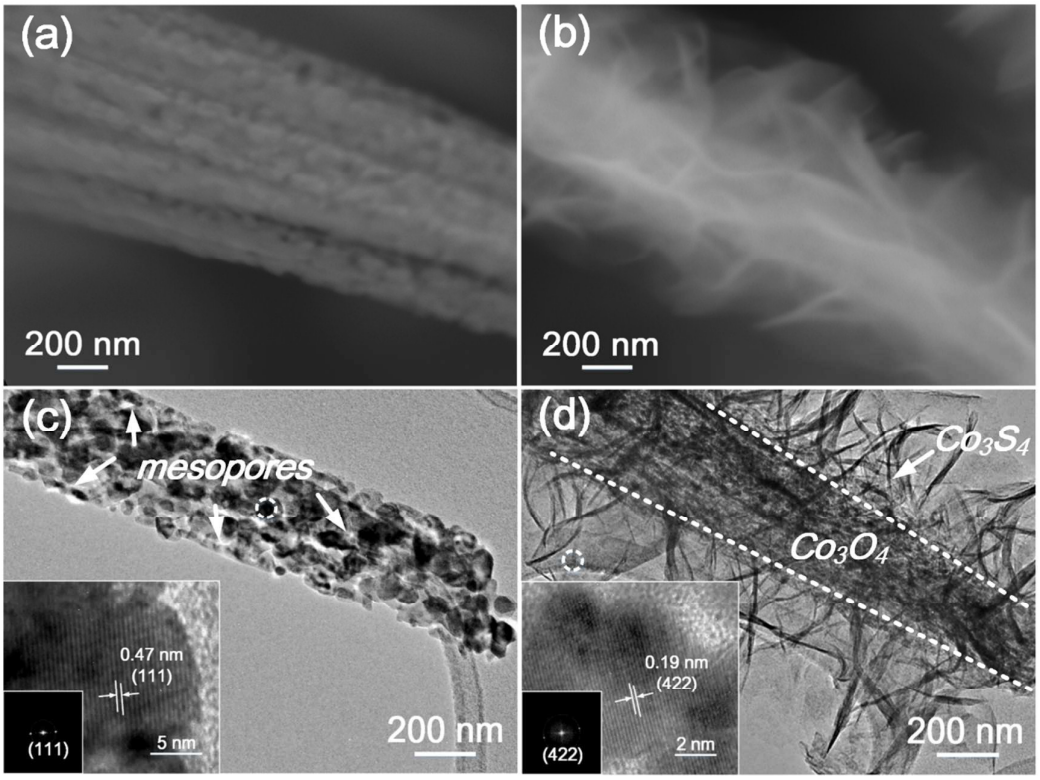

Fig. 2 Enlarged SEM images of Co_3O_4 nanoneedle (a) and Co_3O_4@Co_3S_4 hybrid hierarchical nanostructure (b) on Ni foam; TEM images of porous Co_3O_4 nanoneedle (c) and Co_3S_4 nanowhiskers on Co_3O_4 nanoneedle (d); insets of (c and d) are high-resolution TEM images and FFT patterns of Co_3O_4 and Co_3O_4@Co_3S_4, respectively.

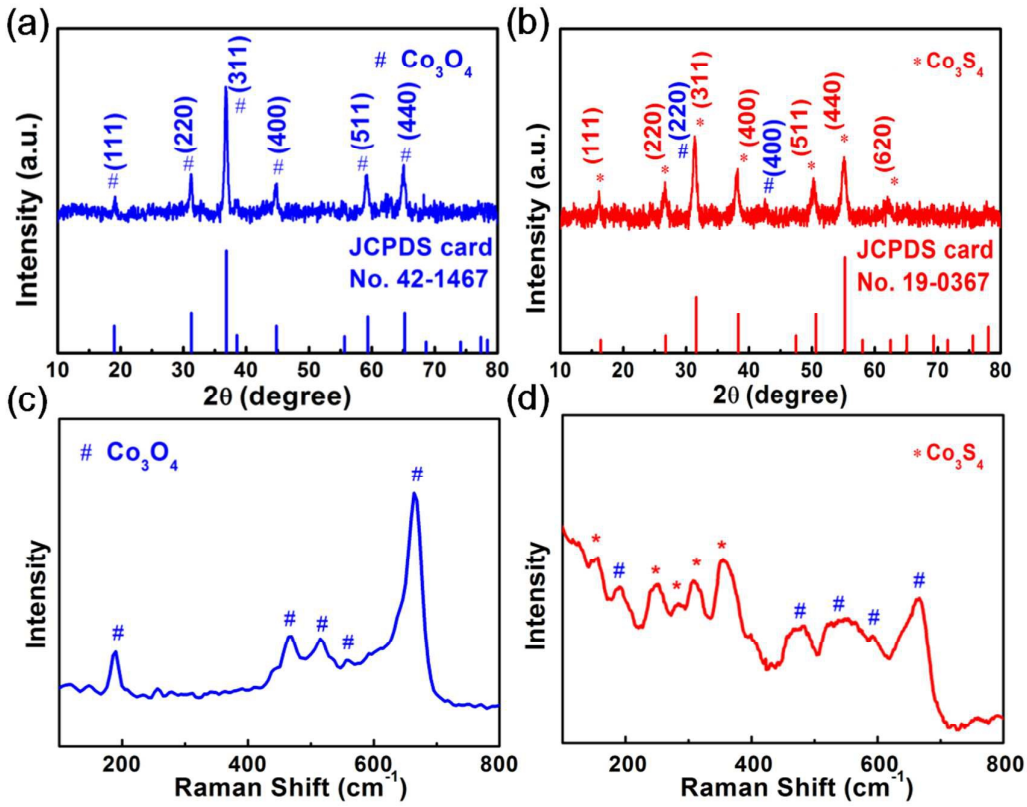

Fig. 3 XRD plots of (a) Co_3O_4 and (b) Co_3O_4@Co_3S_4; Raman spectrum of (c) Co_3O_4 and (d) Co_3O_4@Co_3S_4, respectively.

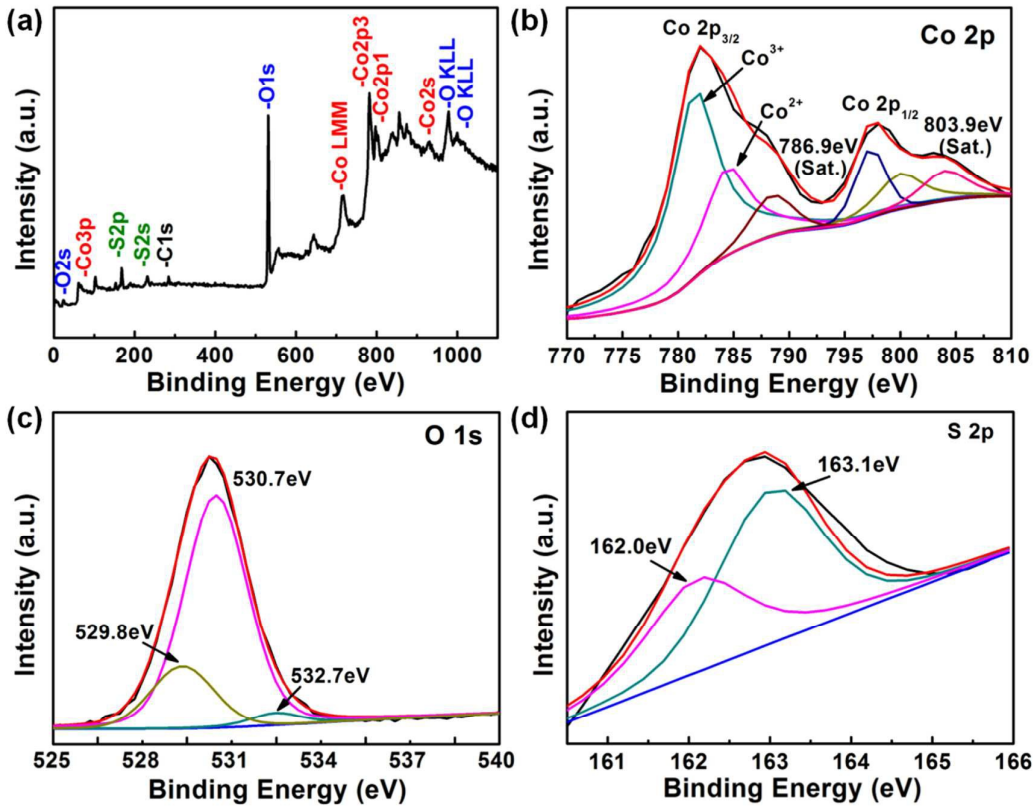

Fig. 4 XPS full-scan spectrum of Co, O, S, and C (a); high-resolution XPS elemental spectrum of Co (b), O (c), and S (d), respectively.

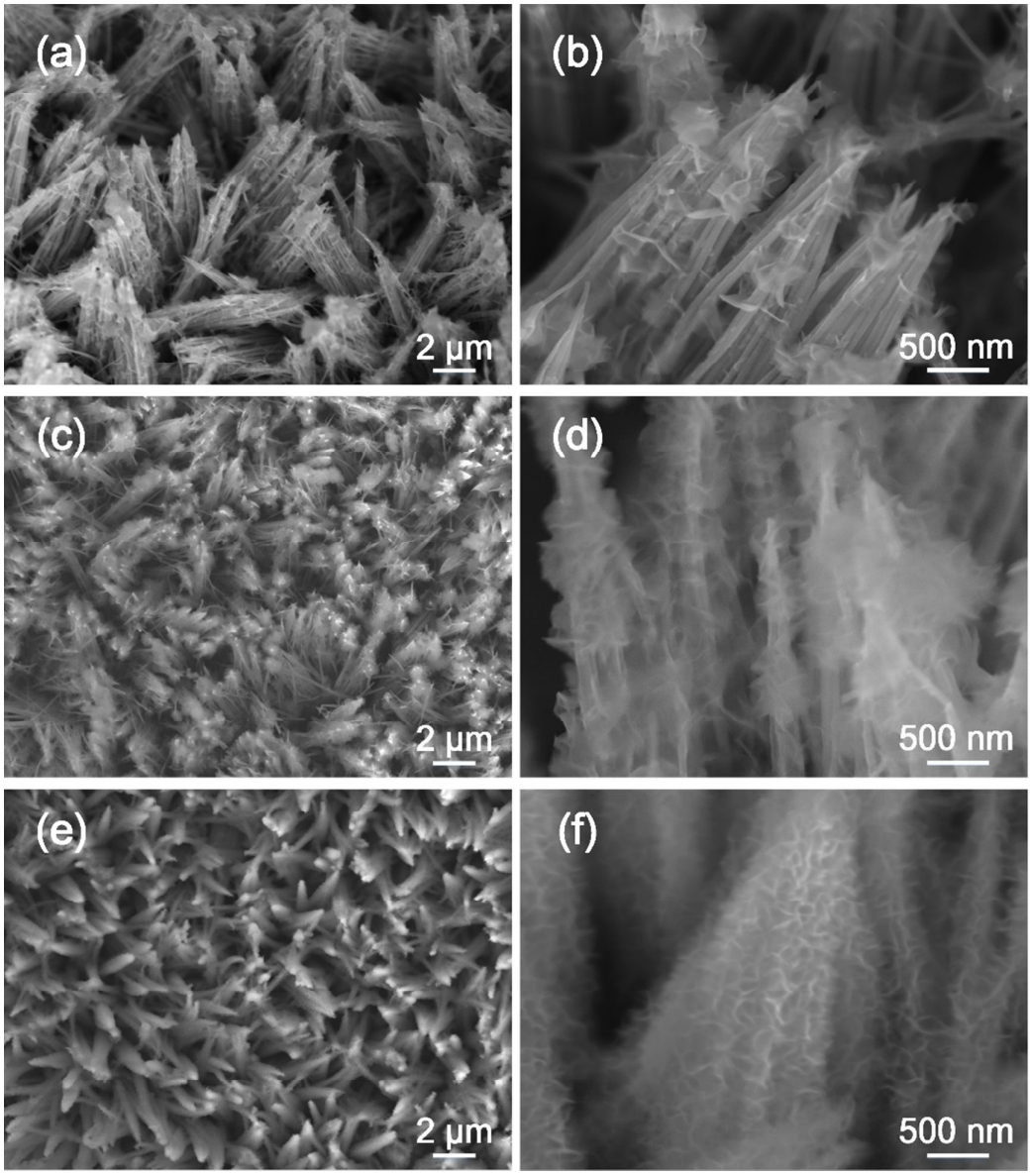

Fig. 5 SEM images of Co_3O_4@Co_3S_4 hybrid hierarchical nanostructure synthesized at different durations, i.e.,12 h (a and b) , 24 h (c and d) , and 36 h (e and f).

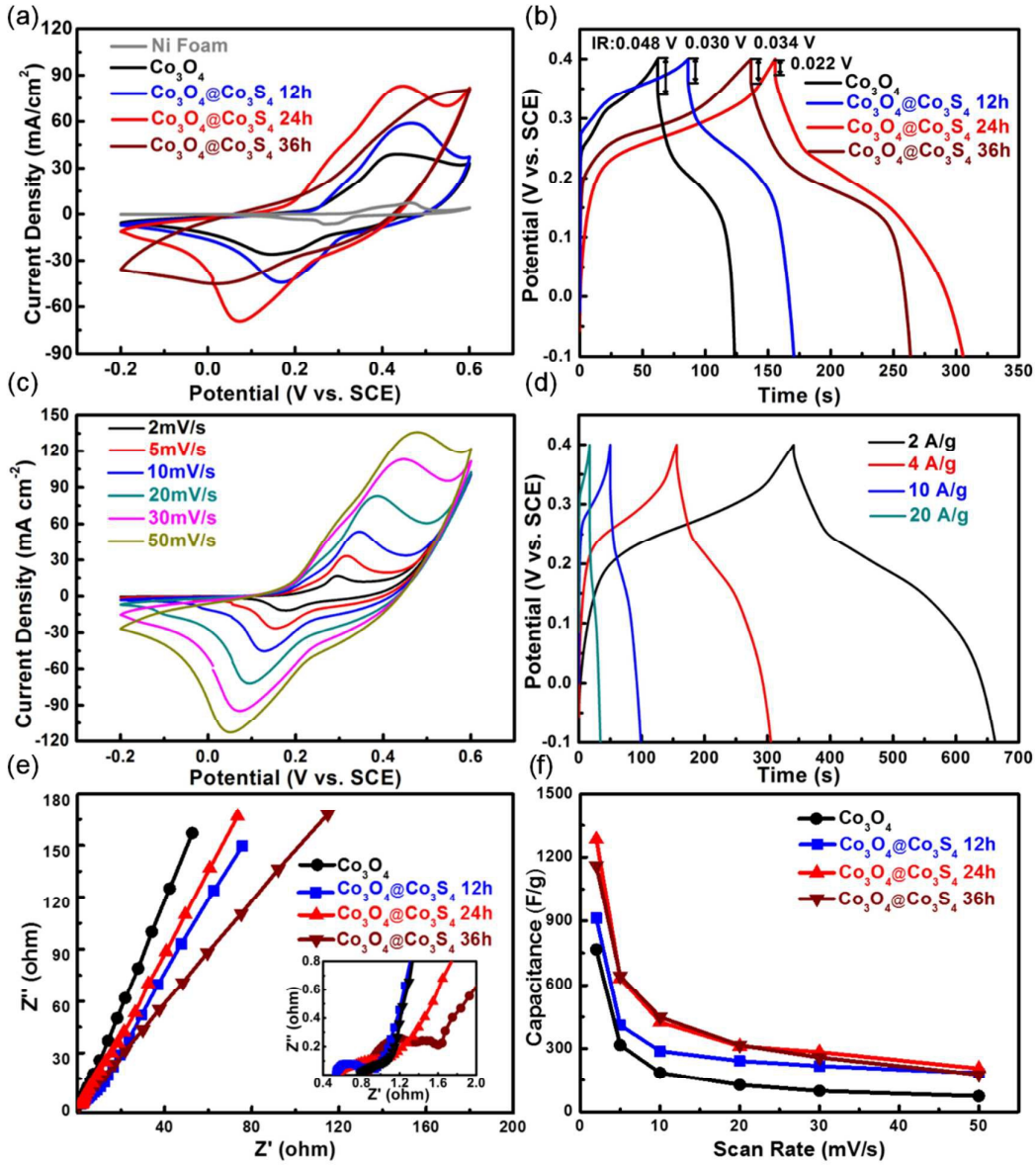

Fig. 6 (a) Comparison of CV and (b) galvanostatic charge–discharge curves for pure Ni foam, Co_3O_4 NNAs, and Co_3O_4@Co_3S_4 NAs at a scan rate of 30 mV s^{-1} and a current density of 4 A g^{-1}, respectively; (c) CV and (d) galvanostatic charge–discharge curves of Co_3O_4@Co_3S_4 NAs prepared at 24 h in the second hydrothermal synthesis process; (e) scan rates dependence of the specific capacitance of Co_3O_4 NNAs, and Co_3O_4@Co_3S_4 NAs electrodes; (f) Nyquist plots of the Co_3O_4 NNAs, and Co_3O_4@Co_3S_4 NAs electrodes at open circuit potential. The inset of (f) is the enlarged EIS of these electrodes at a high frequency range.

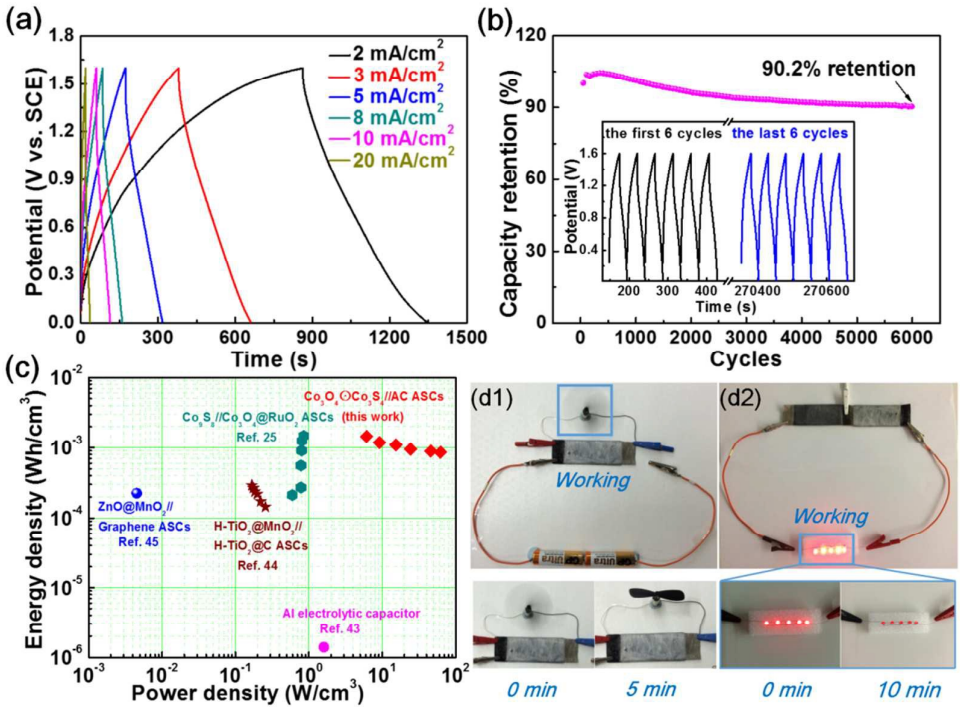

Fig. 7 (a) Galvanostatic charge/discharge curves of the Co_3O_4@Co_3S_4//AC ASCs at various current densities; (b) Cycling performance of Co_3O_4@Co_3S_4//AC ASCs collected at a current density of 20 mA cm^{-2} for 6000 cycles in gel (KOH/PVA) electrolyte, and the inset is galvanostatic charge/discharge curves of the first and the last 6 cycles; (c) The comparison in a Ragone plot of the volumetric energy densities and power densities reported in previous references and those of Co_3O_4@Co_3S_4//AC ASCs; (d1 and d2) photograph of a rotating motor and red LEDs drived by our ASCs device for a period of time.

Table of context

3D hierarchical Co_3O_4@Co_3S_4 nanoarrays as cathode materials for asymmetric pseudocapacitor

Bo Liu,‡[a] Dezhi Kong,‡[a,b] Jun Zhang,[c] Ye Wang,[a] Tupei Chen,[c] Chuanwei Cheng,[b] and Hui Ying Yang[a,*]

[a] Pillar of Engineering Product Development, Singapore University of Technology and Design, 8 Somapah Road, Singapore, 487372

[b] Shanghai Key Laboratory of Special Artificial Microstructure Materials and Technology, School of Physics Science and Engineering, Tongji University, Shanghai 200092, P. R. China

[c] School of Electrical and Electronic Engineering, Nanyang Technological University, Singapore 639798, Singapore

‡ These authors contribute equally to this work.

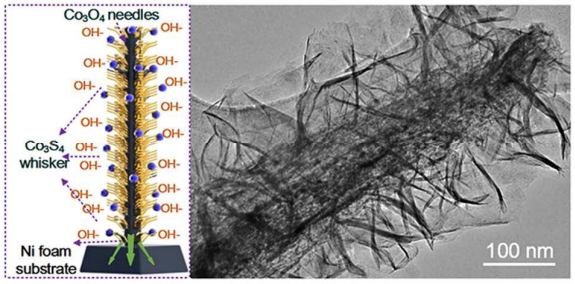

A Co_3O_4@Co_3S_4 nanoarrays electrode is designed by a facile solution synthesis approach and investigated as the cathode material for ASC.